Revisiting causality using stochastics: 2. Applications

Supplementary Information

Demetris Koutsoyiannis[1], Christian Onof[2], Antonis Christofidis[1] and
Zbigniew W. Kundzewicz[3]

[1] Department of Water Resources and Environmental Engineering, School of Civil Engineering, National Technical University of Athens (dk@itia.ntua.gr)

[2] Department of Civil and Environmental Engineering, Faculty of Engineering, Imperial College London

[3] Meteorology Lab, Department of Construction and Geoengineering, Faculty of Environmental Engineering and Mechanical Engineering, Poznan University of Life Sciences, Poznań, Poland

Abstract This report contains Supplementary Information, namely, mathematical derivations, justifications and illustrations, for the paper series *Revisiting causality using stochastics* and in particular its second part, *Applications* (Koutsoyiannis et al., 2022b). It comprises three sections, namely *Assessment of uncertainty in the identification of the impulse response function and its characteristics* (SI2.1), *On high autocorrelations and spurious IRF estimates* (SI2.2), *Parametric approach to identification of the impulse response function* (SI2.3), and *Example of application of the parametric approach to modern temperature and* CO_2 *datasets* (SI2.4). We note that this Supplementary Information (except section SI2.2) was not contained in the initial submission, but was added to address important comments raised by the reviewers.

SI2.1 Assessment of uncertainty in the identification of the impulse response function and its characteristics

While a complete study on the assessment of uncertainty in the identification of the impulse response function (IRF) is not in the scope of the two companion papers, here we provide a preliminary investigation with some first results, leaving more thorough research for future publications. As explained in the main papers (Koutsoyiannis et al., 2022a,b) the method of choice for the uncertainty assessment is the Monte Carlo simulation, as the complexity of the calculations for optimizing the IRF fitting do not allow analytical solutions. Monte Carlo simulation requires a (stochastic) model to be available and it is most reliable if the model is completely known a priori.

For this reason, we have chosen to provide an uncertainty assessment for two of the synthetic case studies contained in the main paper, for which the true IRF is a priori known and could be compared with the estimates. Namely, we have chosen to use the model, comprising the processes, $\underline{x}_\tau$, $\underline{y}_\tau$ and $\underline{u}_\tau$ and equations (3)-(6) of the main paper (Koutsoyiannis et al., 2022b). More specifically, the synthetic case studies of the current investigation are similar to cases #8 and #10 of the main paper (Koutsoyiannis et al., 2022b) but with much higher variance of the noise term $\underline{u}_\tau$, so as to assess the credibility of the methodology under high noise. Namely, we chose the variance of the noise term $\underline{u}_\tau$ twice that of $\underline{x}_\tau$, so that the explained variance of the causal model be around 1/3. It is reminded that both cases #8 and #10 refer to a causal model with an IRF with 21 known weights, where the difference in the two cases relies in unconstrained (#8) or constrained (#10) roughness.

Ten different time series of $\underline{y}_\tau$ were generated, each one with a different realization of $\underline{u}_\tau$ and the same realization of $\underline{x}_\tau$; the latter is kept the same as in the original applications #8 and #10. Then, for each of the 10 time series two IRFs were calculated, one using the nonnegativity constraint only (as in #8) and the other using both the nonnegativity and the roughness constraint (as in #10). The ten IRFs of the former and the latter case are plotted in the left and the right panel of Figure SI2.1, respectively, in the form of spaghetti plots.

As seen in the left panel of Figure SI2.1, the fact that the system is causal is well captured even without using the roughness constraint but the shape of the IRF is too noisy and hence uncertain. If we take the average of the ordinates of the different realizations at each time lag, the resulting curve, also shown in Figure SI2.1, becomes smoother and allows the expectation that the roughness would be eliminated with a large number of Monte Carlo simulations. On the other hand, the right panel shows that, when the roughness is constrained, the uncertainty becomes negligible and the entire shape of the true IRF is well captured even with one simulation. Some small negative bias is seen close to time lag zero, where the second derivative of the true IRF ($g''(h)$) is highest. Also, a small scatter of the IRFs is seen at the highest lags.

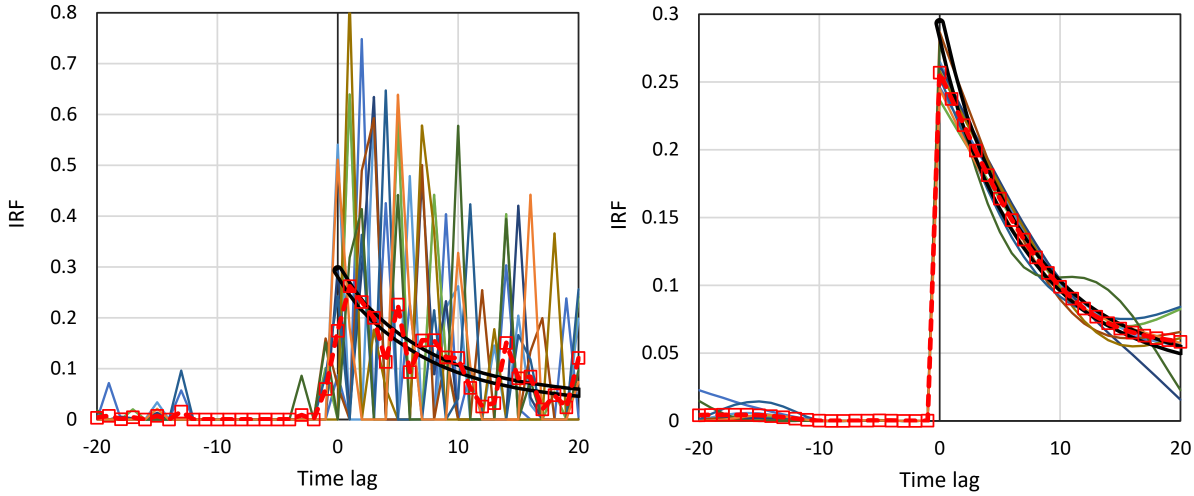

Figure SI2.1 Spaghetti plots of the IRFs for synthetic case studies similar to cases #8 and #10 (left and right, respectively) of the main paper (Koutsoyiannis et al., 2022b) but with variance of the error term $\underline{u}_\tau$ twice that of $\underline{x}_\tau$. Each panel shows ten different IRFs calculated from ten different Monte Carlo realizations of the process $\underline{y}_\tau$, each one with a different realization of the noise $\underline{u}_\tau$, and the same realization of $\underline{x}_\tau$ (see more details in the text). The double black line shows the true IRF and the dotted line with squares the average of ten Monte Carlo realizations.

Furthermore, scatter plots of the characteristic indices of the 20 different IRFs are shown in Figure SI2.2. For each of the ten time series there are two estimates of each index, one estimated using the nonnegativity constraint only (as in #8) and the other using both the nonnegativity and the roughness constraint (as in #10). The scatter plots show the former versus the latter. The left panel of the figure shows the time indices of the IRFs, namely h_c (the time lag maximizing the cross-correlation $r_{yx}(h)$), μ_h (the time average of the function $g(h)$), and $h_{1/2}$ (the median of the function $g(h)$). We note that, among them, h_c is independent of the estimated $g(h)$ as it is directly estimated from the time series. The right panel shows the indices of strength of the potential causal relationship, namely e (the explained variance ratio) and $r_{yx}^2(h_c)$, which again is independent of the estimated $g(h)$ as it is directly estimated from the time series. The quantity $r_{yx}^2(h_c)$ denotes the explained variance in the simplified case that the causality relationship had been determined in terms of an IRF with only one nonnegative ordinate (at lag h_c).

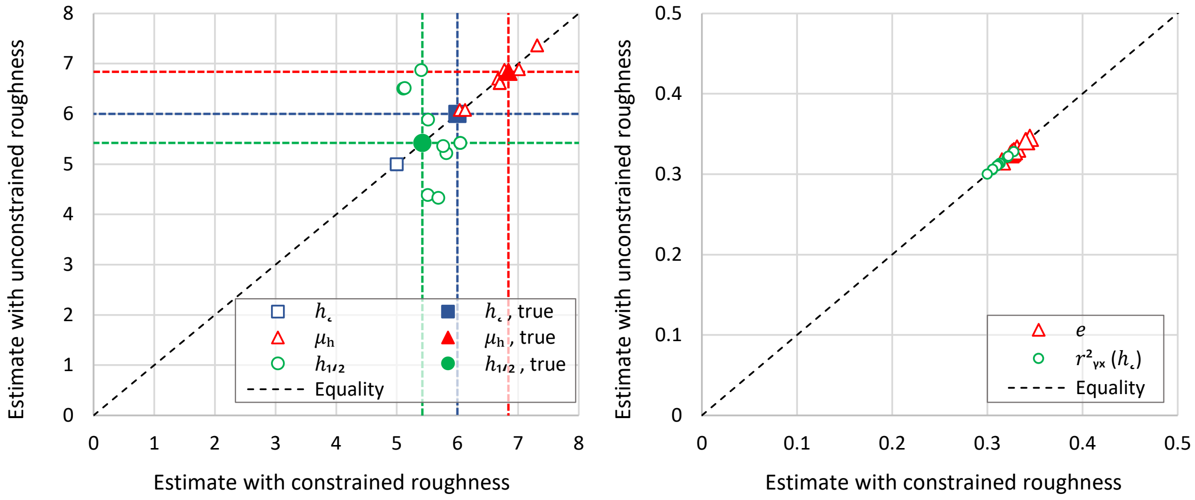

Figure SI2.2 Scatter plots of characteristic indices of the estimated IRFs shown in Figure SI2.1 for the ten generated time series of the processes $\underline{x}_\tau, \underline{y}_\tau$. The coordinates in each plot are the estimates of the indices using the nonnegativity constraint only (vertical axis) and using both the nonnegativity and the roughness constraint (horizontal axis). (Left) Time indices of the IRFs, where h_c is the time lag maximizing the cross-correlation $r_{yx}(h)$, μ_h is the mean (time average) of the function $g(h)$ and $h_{1/2}$ is the median of the function $g(h)$. (Right) Indices of strength of the causal relationship, where e is the explained variance ratio and $r_{yx}^2(h_c)$ is the explained variance in the simplified case that the causality relationship had been determined in terms of an IRF with only one nonnegative ordinate (at lag h_c).

Overall, Figure SI2.2 allows to make the following remarks:

- All indices show a small scatter and thus small uncertainty (coefficient of variation not exceeding 7%), around their true values. This is the case even if the roughness constraint was not used in the estimation of the IRF, despite the erratic appearance of the IRF in this case.
- The estimates are practically equal (plotted over the equality line) in the two estimation options (with or without the roughness constraint); an exception is

seen for the median $h_{1/2}$ only. This illustrates the high robustness in estimating these indices and hence of the identification of the necessary conditions for causality.

- The variation of the estimates of the explained variance ratio e is about the same as that of $r_{yx}^2(h_c)$ (smaller than 3%). As the latter quantity is a characteristic of the time series and is independent of the IRF, this suggests that the estimation of the IRF per se does not increase the uncertainty that is already present because we do not have full information on the processes but only the information contained in the realization thereof (the available time series).

SI2.2 On high autocorrelations and spurious IRF estimates

As stated in the main papers (Koutsoyiannis et al., 2022a,b), high autocorrelation results in increased estimation uncertainty and may even result in spurious causality claims. To illustrate this, we devise a synthetic example, in which the processes $\underline{x}_\tau$ and $\underline{y}_\tau$ are, by construction, independent of each other and with high autocorrelation.

Specifically, two time series x_τ and y_τ, each of length 500, are generated independently from each other. The time series x_τ is constructed by the deterministic rule $x_\tau = 1 + 0.001\tau$. If its values are treated statistically, the resulting autocorrelation estimate is constant for all lags, $\hat{r}_{xx}(h) = 1$. The time series y_τ is generated from a Hurst-Kolmogorov process with Gaussian distribution and with a high Hurst parameter, $H = 0.95$, reflecting strong long-range dependence (LRD). By now, it is well known (e.g. Cohn and Lins, 2005; Koutsoyiannis, 2013) that realizations of processes with LRD look “trendy” even though the processes are stationary. This is evident in Figure SI2.5 (upper), which depicts both time series. Their auto- and cross-correlations, estimated using standard statistical estimators, are shown in Figure SI2.5 (lower). Interestingly, while by construction the cross correlations are $r_{yx}(h) = 0$ for any lag h, their estimates $\hat{r}_{yx}(h)$ appear very high, i.e., 0.46 ± 0.21 in the plotted interval of lag h, $(-100,100)$.

Because of the high cross-correlations, if we estimate the IRF with the proposed method, as seen in Figure SI2.4, spurious Hen-or-Egg (HOE) causality is identified in both directions $\underline{x} \to \underline{y}$ and $\underline{y} \to \underline{x}$. The dominant causality direction appears to be $\underline{y} \to \underline{x}$ with mean lag $\mu_h = 2.6$, median lag $h_{1/2} = 3.2$ and explained variance ratio $e = 0.47$. All these are obviously invalid estimates (as there are no true lags in this case and the true value of the explained variance ratio is $e = 0$), even though the calculations are correct.

Naturally, a remedy in such spurious cases is to reduce the autocorrelations. This becomes possible if instead of the time series x_τ and y_τ we study the differenced time series $\Delta x_\tau \coloneqq x_\tau - x_{\tau-1}$ and $\Delta y_\tau \coloneqq y_\tau - y_{\tau-1}$. Taking the differences is definitely reasonable: if x_τ causes y_τ, then a change in x_τ should cause a change in y_τ. In our example, we will have constant $\Delta x_\tau = 0.001$ and hence the cross-covariances would be zero, which will exclude any causality claim.

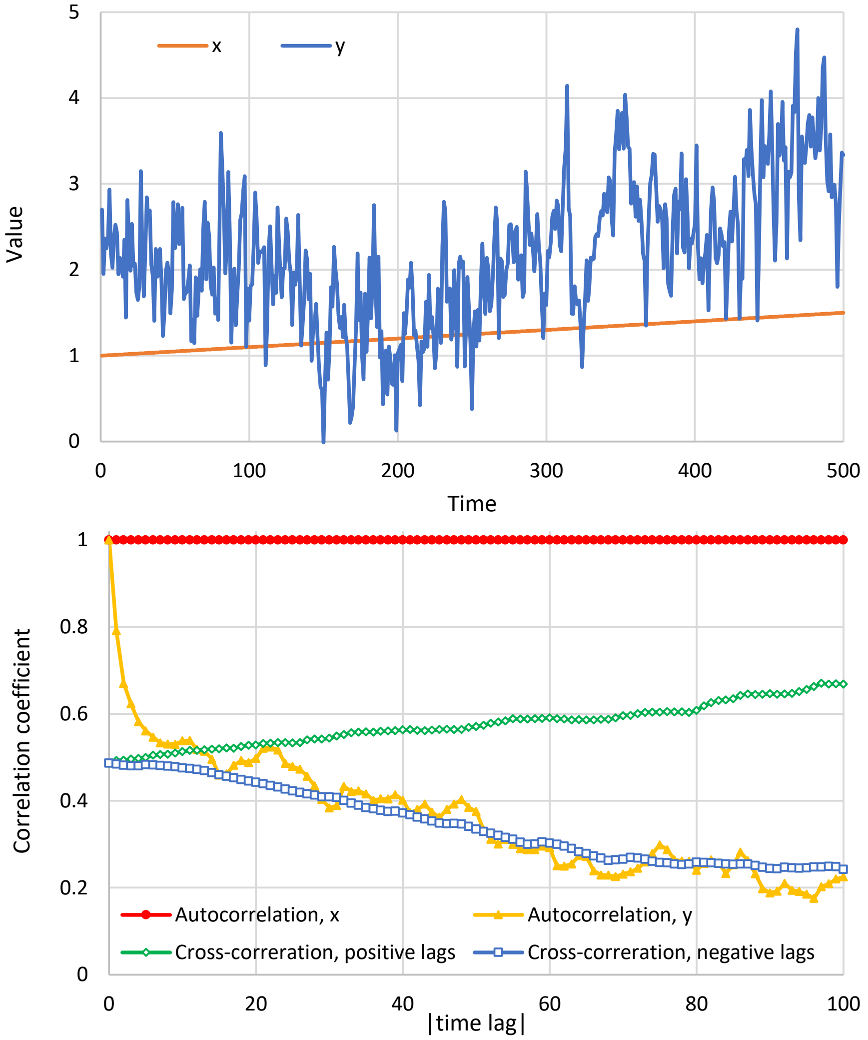

Figure SI2.3 (**upper**) Time series of the synthetic example described in the text. (**lower**) Auto- and cross-correlation function estimates for the two time series.

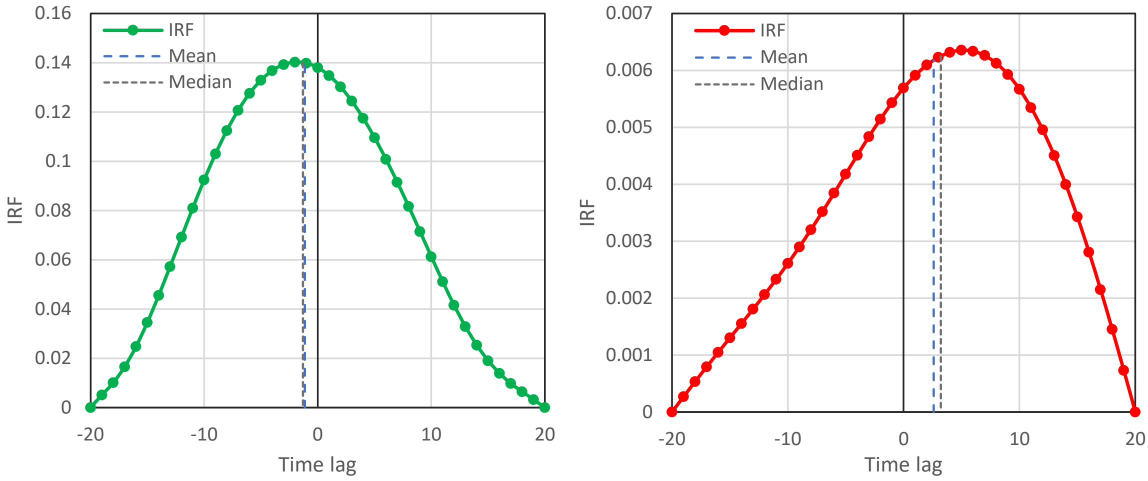

Figure SI2.4 IRFs for the synthetic example of spurious IRF estimation due to high autocorrelation of Figure SI2.3 for causality directions (left) $\underline{x} \to \underline{y}$ and (right) $\underline{y} \to \underline{x}$. For the estimated IRFs the number of weights is $2J + 1$ with $J = 20$.

SI2.3 Parametric approach to identification of the impulse response function

It is reminded that the basic equation for the potentially HOE causal system between the processes $\underline{x}(t)$ and $\underline{y}(t)$ in continuous (natural) time t is:

$$\underline{y}(t) = \int_{-\infty}^{\infty} g(h)\underline{x}(t-h)\mathrm{d}h + \underline{v}(t) \tag{SI2.1}$$

where $g(h)$ is the IRF. While in the two companion papers (Koutsoyiannis et al., 2022a,b) to determine the IRF we have adopted a constrained non-parametric optimization approach, we note that an expression of $g(h)$ through a parametric mathematical equation also constitutes a valid approach. In fact, such an approach has been in use in hydrology since the 1950s. Nash (1959) conceptualized the approach in terms of flow routing through a cascade of linear reservoirs, and demonstrated that, under this assumption, the resulting IRF is a gamma probability density function. At the same time, he gave the relevant tools to estimate the parameters of the function. Koutsoyiannis and Xanthopoulos (1989) heuristically introduced a variety of mathematical expressions, resembling known probability density functions, and outlined parameter estimation approaches using measurements.

Superposition (linear combination) of many parametric functions of a certain type provides a more flexible composite parametric expression for the IRF. This is known as expansion of a function with respect to some basis functions. In our framework, the so-called alpha basis functions, which are often used within neural networks (Rall, 1967; Destexhe et al., 1994; Guo et al., 2019) can be appropriate because of their time-asymmetric shape. The alpha function is a special case of the gamma probability density function for shape parameter equal to 1, i.e.,

$$\alpha_i(h) = \frac{h-h_i}{\eta_i}\exp\left(-\frac{h-h_i}{\eta_i}\right)\mathrm{U}\left(\frac{h-h_i}{\eta_i}\right) \tag{SI2.2}$$

where h_i and η_i are parameters, $i = 1, \dots, I$, is an index and U denotes the (Heaviside) unit step function. Given the I elementary functions, the IRF is expressed by the composite expression

$$g(h) = \sum_{i=1}^{I} \theta_\iota\, \alpha_i(h) \tag{SI2.3}$$

where θ_i are additional parameters. Note that our basis function is either potentially causal for $\eta_i > 0, h_i \geq 0$ or potentially anticausal for $\eta_i < 0, h_i \leq 0$, while the superposition of several such basis functions could well lead to potential HOE causality. The scheme has, thus, $3I$ parameters, which can be determined by minimizing the fitting error, again using a nonlinear solver, similar to what is described in the companion paper (Koutsoyiannis et al. 2022a). We recall from there that in order to move from continuous time to discrete time, we need first to determine a double integral, which for our ith basis function is $A_i(b) \coloneqq \int_{-\infty}^{b} \int_{-\infty}^{a} \alpha_i(h)\mathrm{d}h\, \mathrm{d}a$ and can be easily evaluated to:

$$A_i(b) = \eta_i^2 \left(\frac{b - h_i}{\eta_i} - 2 + e^{-\frac{b-h_i}{\eta_i}} \left(2 + \frac{b - h_i}{\eta_i} \right) \right) \mathrm{U}\left(\frac{b - h_i}{\eta_i} \right) \tag{SI2.4}$$

By virtue of equation (22) of the companion paper (Koutsoyiannis et al., 2022a) we find the discretized version of $\alpha_i(h)$ as:

$$\alpha_{ij} = \frac{A_j\big((j-1)D\big) - 2A_j(jD) + A_j\big((j+1)D\big)}{D} \tag{SI2.5}$$

where for convenience we have restricted h_i/D to be an integer. Finally, the discrete-time IRF is

$$g_j = \sum_{i=1}^{I} \theta_\iota\, \alpha_{ij} \tag{SI2.6}$$

Hence the problem is to determine the parameters $h_i\ \eta_i, \theta_\iota, i = 1, \dots, I$ by optimization, a task that can be easily tackled by any solver.

SI2.4 Example of application of the parametric approach to modern temperature and CO$_2$ datasets

Here we perform three pairs of applications of the parametric framework described in section SI2.3 to one of the data sets, namely the modern temperature and CO$_2$ data, for which the applications of the nonparametric framework #23 and #24 have been conducted in the main paper (Koutsoyiannis et al., 2022b).

In the first pair of applications, denoted in Table SI2.1 and Figure SI2.5 as #SI1 for causality direction $\Delta T \rightarrow \Delta\ln[\mathrm{CO_2}]$ and #SI2 for causality direction $\Delta\ln[\mathrm{CO_2}] \rightarrow \Delta T$, four basis functions are used without any constraint. While the main direction of causality becomes clear again, i.e. $\Delta T \rightarrow \Delta\ln[\mathrm{CO_2}]$ as in the #23 of the main paper (Koutsoyiannis et al., 2022b), interestingly, some negative parts of IRFs appear in Figure SI2.5 for this pair of applications. We attribute them to statistical effects. If one assumed that these reflect some reality (such as an oscillational causality behaviour), one would have to accept some paradoxes. For example, with reference to the case $\Delta\ln[\mathrm{CO_2}] \rightarrow \Delta T$, in which $g(h)$ is negative for most possible lags (upper right corner of Figure SI2.5), one would have to accept that an increase of CO$_2$ concentration in the past would result in a decrease of temperature in the present and future.

Recalling from the main papers (Koutsoyiannis et al., 2022a,b) that oscillatory behaviours are mostly spurious, we proceed to a second pair of applications imposing the nonnegativity constraint, namely #SI3 for causality direction $\Delta T \rightarrow \Delta\ln[\mathrm{CO_2}]$ and #SI4 for causality direction $\Delta\ln[\mathrm{CO_2}] \rightarrow \Delta T$. Again, we use four basis functions but we note that eventually the solver annihilated one of them (overparameterization). Now everything seems reasonable, and again the main direction of causality is clearly $\Delta T \rightarrow \Delta\ln[\mathrm{CO_2}]$ as in all similar applications. All summary characteristics are very close to the ones of the nonparametric approach, as seen in Table SI2.1.

Finally, the most parsimonious case with only one basis function is also considered and shown in Table SI2.1, namely #SI5 for causality direction $\Delta T \rightarrow \Delta\ln[\mathrm{CO_2}]$ and #SI6 for causality direction $\Delta\ln[\mathrm{CO_2}] \rightarrow \Delta T$, as well as in Figure SI2.5. Even in this case the results are satisfactory and agree with those of all other cases, with a noticeable but very small decrease in the explained variance ratio.

Overall, these additional applications confirm the robustness and reliability of the proposed framework and, at the same time, strengthen the validity of the results reported in the main paper (Koutsoyiannis et al., 2022b).

Table SI2.1 Summary indices for the results of the additional case studies elaborated for the modern temperature and $\mathrm{CO_2}$ data (time step: month). For comparison, the results of the nonparametric approach (cases #23 and #24) are also copied from the main paper in the end of the table. The h_c is the time lag maximizing the cross-covariance $c_{yx}(h)$, or equivalently the cross-correlation $r_{yx}(h) \coloneqq c_{yx}(h)/\sqrt{c_{xx}(0)c_{yy}(0)}$; μ_h is the mean (time average) of the function $g(h)$; $h_{1/2}$ is the median of the function $g(h)$; e is the explained variance ratio; and ε is the roughness ratio.

Case	**Direction**	h_c	μ_h	$h_{1/2}$	$r_{yx}(h_c)$	e	ε	#
Four basis functions, no constraint	$\Delta T \rightarrow \Delta\ln[\mathrm{CO_2}]$	5	9.08	– *	0.480	0.32	0.098	SI1
	$\Delta\ln[\mathrm{CO_2}] \rightarrow \Delta T$	–5	–59.5	– *	0.480	0.42	0.0024	SI2
Four basis functions, nonnegativity constraint	$\Delta T \rightarrow \Delta\ln[\mathrm{CO_2}]$	5	7.81	5.33	0.480	0.31	0.069	SI3
	$\Delta\ln[\mathrm{CO_2}] \rightarrow \Delta T$	–5	–5.40	–4.98	0.480	0.24	0.022 §	SI4
One basis function, no constraint	$\Delta T \rightarrow \Delta\ln[\mathrm{CO_2}]$	5	7.10	6.23	0.480	0.29	0.0031	SI5
	$\Delta\ln[\mathrm{CO_2}] \rightarrow \Delta T$	–5	–5.38	–5.05	0.480	0.24	0.048	SI6
Nonparametric approach, results copied from the main paper, #23 and #24	$\Delta T \rightarrow \Delta\ln[\mathrm{CO_2}]$	5	7.70	6.35	0.480	0.31	1.3×10^{-5} §	SI7
	$\Delta\ln[\mathrm{CO_2}] \rightarrow \Delta T$	–5	–5.67	–5.49	0.480	0.23	7.3×10^{-4} §	SI8

* We have not defined the median in cases that include negative values of g_j.

§ The roughness was calculated without considering the second derivative at zero.

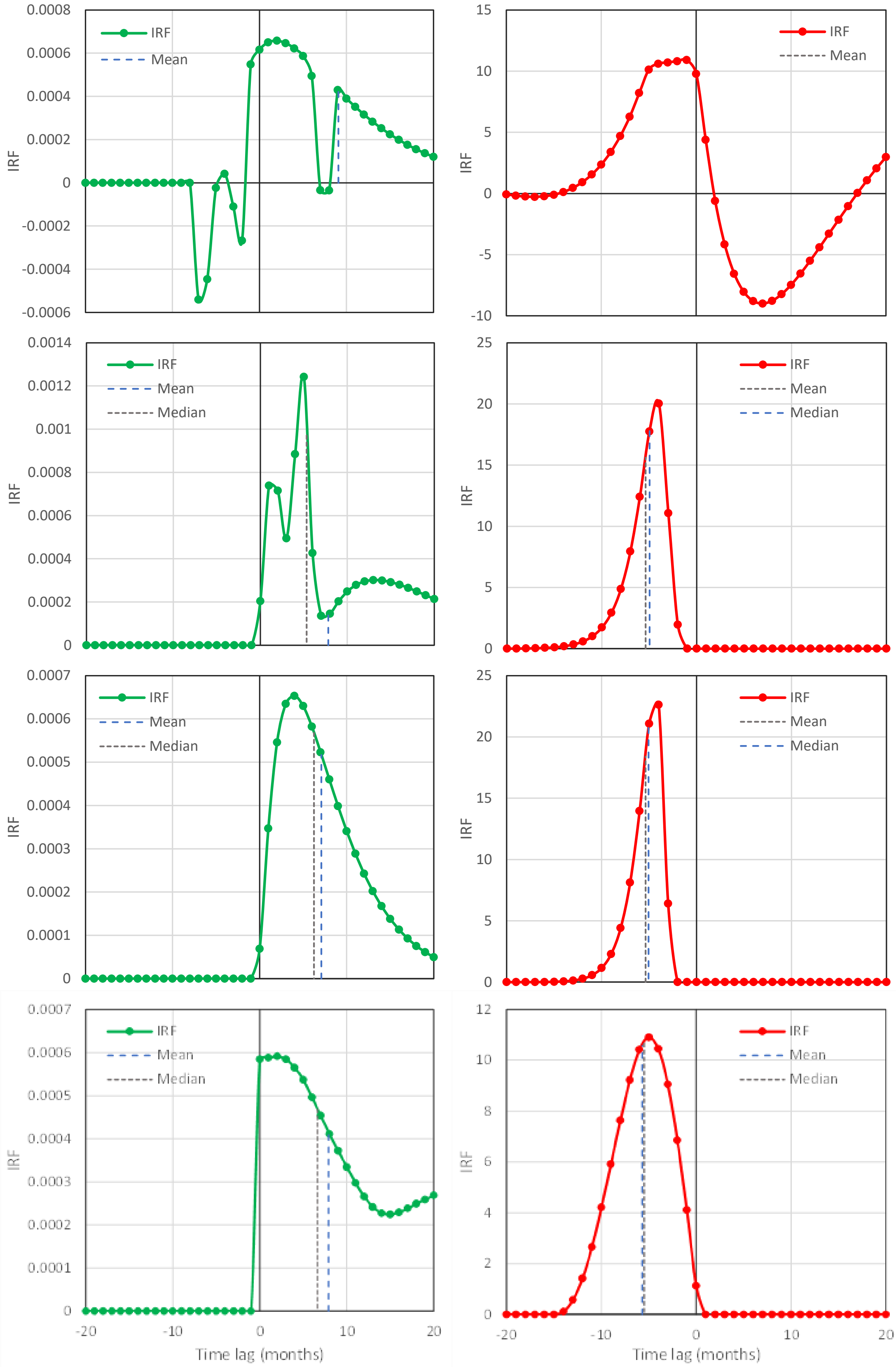

Figure SI2.5 IRFs for of temperature – CO_2 concentration based on the modern time series. Left column: Causality direction $\Delta T \rightarrow \Delta\ln[CO_2]$; right column: causality direction $\Delta\ln[CO_2] \rightarrow \Delta T$. 1st row: applications #SI1 and #SI2 (four basis functions, no constraint); 2nd row: applications #SI3 and #SI4 (four basis functions, nonnegativity constraint); 3rd row: applications #SI5 and #SI6 (one basis function, no constraint); 4th row: applications #SI7 and #SI8 (nonparametric approach, results copied from main paper, #23 and #24).

Acknowledgments: Most of the material in this Supplementary Information was not contained in the initial submission, but was added to address important issues raised by the reviewers. We thank the two anonymous reviewers for their comments and suggestions, which triggered these additional analyses, thus helping us to enhance the validity of our methodology and results.

Funding: This research received no external funding but was motivated by the scientific curiosity of the authors.

Conflicts of Interest: We declare no conflict of interest.

References

Cohn, T.A., and Lins, H.F., 2005. Nature's style: Naturally trendy, *Geophysical Research Letters*, 32(23), L23402, doi: 10.1029/2005GL024476.

Destexhe, A., Mainen, Z.F. and Sejnowski, T.J., 1994. Synthesis of models for excitable membranes, synaptic transmission and neuromodulation using a common kinetic formalism. *Journal of Computational Neuroscience*, 1(3), 195-230.

Guo, Y., Wang, L., Li, Y., Luo, J., Wang, K., Billings, S.A. and Guo, L., 2019. Neural activity inspired asymmetric basis function TV-NARX model for the identification of time-varying dynamic systems. *Neurocomputing*, 357, pp.188-202.

Koutsoyiannis, D., 2013. LTP: Looking Trendy—Persistently, *Climate Dialogue*, doi: 10.13140/RG.2.2.13070.36169.

Koutsoyiannis, D., Onof, C. Christofidis, A., & Kundzewicz, Z. W. 2022a. Revisiting causality using stochastics: 1. Theory, *Proceedings of the Royal Society A*, in review.

Koutsoyiannis, D., Onof, C. Christofidis, A., & Kundzewicz, Z. W. 2022b. Revisiting causality using stochastics: 2. Applications, *Proceedings of the Royal Society A*, in review.

Koutsoyiannis, D., and Xanthopoulos, T., 1989. On the parametric approach to unit hydrograph identification. *Water Resources Management*, 3 (2), 107–128, doi: 10.1007/BF00872467.

Nash, J.E. 1959 Systematic determination of unit hydrograph parameters. *J. Geoph. Res.* **64**(1), 111-115.

Rall, W., 1967. Distinguishing theoretical synaptic potentials computed for different soma-dendritic distributions of synaptic input. *Journal of Neurophysiology*, 30(5), 1138-1168.